

## Exact Calculation of Nonideal Fields Demonstrates Dominance of Injection in Relativistic Reconnection

SAMUEL R. TOTORICA,<sup>1,2,3</sup> SEIJI ZENITANI,<sup>4,5</sup> SHUICHI MATSUKIYO,<sup>6,7</sup> MAMI MACHIDA,<sup>8,9</sup> KAZUHIRO SEKIGUCHI,<sup>8</sup> AND AMITAVA BHATTACHARJEE<sup>1,8,3,10</sup>

<sup>1</sup>*Department of Astrophysical Sciences, Princeton University, Princeton, New Jersey 08544, USA*

<sup>2</sup>*Department of Astro-fusion Plasma Physics (AFP), Headquarters for Co-Creation Strategy, National Institutes of Natural Sciences, Tokyo 105-0001, Japan*

<sup>3</sup>*Princeton Center for Heliophysics, Princeton, New Jersey 08543, USA*

<sup>4</sup>*Space Research Institute, Austrian Academy of Sciences, Graz 8042, Austria*

<sup>5</sup>*Research Center for Urban Safety and Security, Kobe University, 1-1 Rokkodai-cho, Nada-ku, Kobe 657-8501, Japan*

<sup>6</sup>*Faculty of Engineering Sciences, Kyushu University 6-1 Kasuga-Koen, Kasuga, Fukuoka 816-8580, Japan*

<sup>7</sup>*International Research Center for Space and Planetary Environmental Science, Kyushu University, Motoooka, Nishi-Ku, Fukuoka 819-0395, Japan*

<sup>8</sup>*Department of Astro-fusion Plasma Physics (AFP), Headquarters for Co-Creation Strategy, National Institute of Natural Sciences, Tokyo 105-0001, Japan*

<sup>9</sup>*Division of Science, National Astronomical Observatory of Japan, 2-21-1 Osawa, Mitaka, Tokyo 181-8588, Japan*

<sup>10</sup>*Princeton Plasma Physics Laboratory, Princeton University, Princeton, New Jersey 08540, USA*

(Dated: September 18, 2023; Received September 18, 2023; Revised; Accepted)

Submitted to ApJL

### ABSTRACT

Magnetic reconnection is an important source of energetic particles in systems ranging from astrophysics to the laboratory. The large separation of spatiotemporal scales involved makes it critical to determine the minimum physical model containing the necessary physics for modeling particle acceleration. By resolving the energy gain from ideal and nonideal magnetohydrodynamic electric fields self-consistently in kinetic particle-in-cell simulations of reconnection, we conclusively show the dominant role of the nonideal field for the early stage of energization known as injection. The importance of the nonideal field increases with magnetization, guide field, and in three-dimensions, indicating its general importance for reconnection in natural astrophysical systems. We obtain the statistical properties of the injection process from the simulations, paving the way for the development of extended MHD models capable of accurately modeling particle acceleration in large-scale systems. The novel analysis method developed in this study can be applied broadly to give new insight into a wide range of processes in plasma physics.

*Keywords:* magnetic reconnection, nonthermal particle acceleration

### 1. INTRODUCTION

Magnetic reconnection is known to be an important mechanism for converting magnetic field energy into plasma heating and nonthermal energetic particles in space physics and astrophysics [Zweibel & Yamada \(2009\)](#); [Yamada et al. \(2010\)](#); [Ji & Daughton \(2011\)](#). For the relativistic magnetic field strengths of highly magnetized astrophysical objects, reconnection has been shown to be an efficient mechanism for producing power law distributions of energetic particles through the use of fully kinetic particle-in-cell (PIC) simulations [Zenitani & Hoshino \(2001\)](#); [Sironi & Spitkovsky \(2014\)](#); [Guo et al. \(2014\)](#). However, due to computational expense, fully kinetic simulations can only model small system sizes and short timescales, and it is a major challenge to relate such simulations to the global scales of realistic objects. An important question for studying particle acceleration from reconnection is whether fully kinetic

simulations are necessary, or whether the important acceleration mechanisms can be captured in reduced models such as magnetohydrodynamics (MHD). The answer to this question has deep implications for the modeling of astrophysical objects, as only MHD models (in their traditional or extended forms) can feasibly capture the global scales of realistic systems. Nonideal electric fields, defined as those that are not captured in ideal MHD, are strongest inside the current sheet due to kinetic effects. Recent studies have come to differing conclusions on the importance of these fields in the relativistic regime, with arguments that these fields can be neglected Guo et al. (2019, 2022), or in contrast, that they are crucial for giving particles their initial boost to relativistic energies which injects them into Fermi acceleration processes Sironi (2022). The majority of the overall particle energy gain is believed to come from Fermi acceleration by ideal electric fields associated with the merging and contraction of plasmoids that are captured in ideal MHD Drake et al. (2006), however, this has not been systematically tested. Particles continue to be exposed to nonideal fields at all stages of their evolution, for example in secondary current sheets that form between merging plasmoids Oka et al. (2010), polarization electric fields from charge separation, or from the rich variety of kinetic plasma waves that can be excited in the current sheet.

Past work analyzing the role of nonideal fields in magnetic reconnection has almost exclusively relied on approximate criteria, by focusing on regions where the electric field magnitude exceeds the magnetic field ( $|\mathbf{E}| > |\mathbf{B}|$ ) for antiparallel reconnection, or regions where the electric field has a component parallel to the magnetic field ( $\mathbf{E} \cdot \mathbf{B} \neq 0$ ) for reconnection with a finite guide field. While the ideal MHD condition  $\mathbf{E} = -\mathbf{v}_{fl} \times \mathbf{B}/c$  (where  $\mathbf{v}_{fl}$  is the plasma fluid velocity) is manifestly violated in these two cases, these sufficient but not necessary conditions do not capture the full nonideal field which is given exactly by  $\mathbf{E} + \mathbf{v}_{fl} \times \mathbf{B}/c$ . The exact nonideal field can be obtained in postprocessing at a given timestep from standard kinetic PIC simulation outputs, however, accessing the nonideal field during the runtime of a PIC simulation requires a significant modification of the code with many subtleties that must be considered. Furthermore, the necessity of calculating an additional four quantities from the simulation particles (three fluid velocity components and the particle number density for each species) to obtain the nonideal field adds a significant computational burden to an electromagnetic PIC simulation, where three current density components alone are sufficient to advance the electromagnetic fields to the next timestep. For these reasons, approximate conditions have remained the standard for investigating nonideal effects.

However, Figure 1 (a) shows why it is critical to calculate the exact nonideal electric field for the purpose of investigating the limitations of MHD. This figure shows the separation of the ideal (top) and nonideal (middle) electric fields in the out-of-plane direction along with the binary result of the  $|\mathbf{E}| > |\mathbf{B}|$  condition (bottom) calculated from a standard relativistic reconnection PIC simulation, zoomed into the diffusion region. The nonideal component has a characteristic magnitude that is typically around 5 times smaller than that of the ideal component, and shows an intricate structure extending throughout the current sheet and into the reconnection outflows. Importantly, as seen in the bottom plot of Figure 1 (a), there are significant contributions even in regions where the magnitude of the electric field does not exceed that of the magnetic field, demonstrating the severe limitation of the simplified  $|\mathbf{E}| > |\mathbf{B}|$  condition. The nonideal field around X-points has been extensively studied Hesse et al. (2011), however the physical mechanisms underlying the nonideal fields that are seen further downstream are not yet well understood.

In this Letter, we present the first analysis resolving energization from ideal and nonideal fields in magnetic reconnection self-consistently for every particle at every timestep in a PIC simulation. By determining the relative roles of the ideal and nonideal fields in the early stages of particle energization, we conclusively show the importance of the nonideal field in the injection process and determine a characteristic injection energy. By analyzing a set of simulations with various parameters of astrophysical relevance, we find the importance of the nonideal field increases with magnetization, guide field strength, and with the inclusion of three-dimensional effects, indicating its general relevance for astrophysical systems in nature. Numerical convergence studies show the robustness of the results and validity of the analysis method, which can now be applied to give new insight into a wide range of scenarios in plasma physics. Finally, we obtain statistical properties of the injection process, and discuss prospects for embedding them into extended MHD simulations which could enable the modeling of astrophysical particle acceleration in large-scale systems.

## 2. METHODS

### 2.1. Simulation setup

To model relativistic reconnection we use OSIRIS, a state-of-the-art, fully relativistic and electromagnetic PIC code Fonseca et al. (2002, 2008, 2013). The simulations are initialized as force-free current sheets Kilian et al. (2020), with

magnetization ranging from  $\sigma = 12.5 - 200$  and guide field ranging from  $B_G/B_0 = 0 - 1$ , where  $\sigma = B_0^2/4\pi nmc^2$  and  $B_0$  is the asymptotic value of the initial reconnecting field. The plasma consists of electron-positron pairs that are initially relativistically cold ( $u_{th}/c = 10^{-4}$ ), and reconnection starts from thermal noise in the system with no imposed perturbation. (Unlike the case of an ionic plasma, the characteristic spatial scales of oppositely charged particles are identical in a pair plasma.) The initial current sheet half-widths are  $\delta/(c/\omega_p) = 5$  for simulations with  $\sigma = 12.5 - 50$ , and  $\delta/(c/\omega_p) = 7, 10$  for simulations with  $\sigma = 100, 200$ , respectively. Particles with initial positions within  $\pm 4\delta$  from the center of the layer are excluded from all analysis to eliminate effects from the initial current supporting the magnetic field reversal. Unless otherwise stated, for two-dimensional (2D) simulations the number of particles-per-cell is  $n_{ppc} = 16$  per-species, the spatial and temporal resolutions are  $\Delta x/(c/\omega_p) = 0.25$  and  $\omega_p\Delta t = 0.175$ , and the domain size is  $L_x/(c/\omega_p) = L_y/(c/\omega_p) = 1000$ , where  $x$  and  $y$  are the reconnection outflow and inflow directions, respectively. For three-dimensional (3D) simulations,  $n_{ppc} = 8$  per-species,  $\Delta x/(c/\omega_p) = 0.25$ ,  $\omega_p\Delta t = 0.143$ ,  $L_x/(c/\omega_p) = L_y/(c/\omega_p) = 1000$ , and  $L_z/(c/\omega_p) = 150$ . The  $y$  boundaries are conducting for fields and reflecting for particles, and the  $x$  and  $z$  boundaries are periodic. Cubic particle shapes are used to interpolate between particle and grid quantities for all simulations. In the following analysis, particle energies are normalized to  $mc^2$ .

## 2.2. A new analysis method

To analyze the nonideal electric field, we have modified OSIRIS to separate the ideal and nonideal components of the electric field at every timestep in the simulation. First, the plasma fluid velocity is calculated as the velocity of the Eckart frame Zenitani (2018) (where the particle flux vanishes) relative to the lab frame, on a discrete grid from the positions and time-centered velocities of all of the particles in the simulation as  $\mathbf{v}_{fl}(\mathbf{X}_i) = \left( \sum_{e^-,e^+} \sum_{n=1}^{N_p} S(\mathbf{x}_n - \mathbf{X}_i) m\mathbf{u}_n/\gamma_n \right) / \left( \sum_{e^-,e^+} \sum_{n=1}^{N_p} S(\mathbf{x}_n - \mathbf{X}_i) m \right)$ , where  $S$  is the particle shape factor Birdsall & Langdon (1985). Due to the time staggering characteristic of the leapfrog particle pusher used in PIC simulations, it is necessary to retain the particle velocity from the previous timestep to calculate the time-centered velocity. The fluid velocity and magnetic field are then interpolated to the position of the particle, allowing a decomposition of the electric field acting on the particle into ideal and nonideal components as  $\mathbf{E}_I = -\mathbf{v}_{fl} \times \mathbf{B}/c$  and  $\mathbf{E}_N = \mathbf{E}_T - \mathbf{E}_I$ , respectively. The interpolation between particle and grid quantities used at all steps is the same as that in the simulation (cubic). With access to the ideal and nonideal components of the electric field, their contributions to the energy gain of a particle in a given timestep can be calculated as  $\Delta\epsilon_N = q\mathbf{E}_N \cdot \mathbf{v}_{particle}\Delta t$ , and similarly for the ideal component. Finally, a normalization factor is applied to ensure the sum of the energy gain from the ideal and nonideal components is exactly equal to the total energy gain of the particle between timesteps, however we have found the results are not sensitive to the small discretization error introduced without normalization. We track the cumulative ideal and nonideal energization for every particle at every timestep in the simulation to study their relative importance in different acceleration processes.

## 2.3. Testing injection

To study the critical problem of injection, we isolate the contribution of the nonideal field in the early stages of particle energization. Figure 1 shows an example trajectory of a representative simulation particle plotted over the out-of-plane component of the nonideal electric field in (b), along with the energy gained from the nonideal ( $\epsilon_N(t) = \sum_0^t \Delta\epsilon_N$ ) and ideal ( $\epsilon_I(t) = \epsilon_T(t) - \epsilon_T(0) - \epsilon_N(t)$ , where  $\epsilon_T(t)$  is the particle's total energy with initial energy  $\epsilon_T(0) \ll \sigma$ ) electric fields as a function of time in (c). The particle enters the current sheet and first becomes strongly energized by the nonideal component of the electric field. After reaching an energy of  $\approx 0.4\sigma$ , the ideal component of the electric field takes over as the dominate source of energization. Figure 1 (d) shows a plot of  $\epsilon_N/\sigma$  versus the total particle energy  $\epsilon_T/\sigma$  in blue. During the initial stage,  $\epsilon_N \approx \epsilon_T$ , indicating the acceleration is dominantly nonideal. To determine the importance of the nonideal field in the early stages of energization we first define a threshold energy  $\epsilon^*$ . The fraction of energy gained from the nonideal field when the particle reaches the threshold energy,  $(\epsilon_N/\epsilon_T)|_{\epsilon_T=\epsilon^*}$ , gives a quantified measure of the importance of the nonideal field for acceleration below particle energies  $\epsilon^*$ . Figure 1 (d) shows the calculation of this quantity for the particle trajectory under consideration with a threshold set to be  $\epsilon^* = \sigma/4$ . In this case  $(\epsilon_N/\epsilon_T)|_{\epsilon_T=\epsilon^*} \approx 0.8$ , indicating the nonideal field was primarily responsible for bringing the particle to the energy of  $\sigma/4$ . Calculating  $(\epsilon_N/\epsilon_T)|_{\epsilon_T=\epsilon^*}$  for all particles in a simulation and for various values of  $\epsilon^*$  allows a statistical determination of the role of the nonideal field in various energy ranges, and in particular its role during particle injection when  $\epsilon^*$  is chosen to be suitably small.

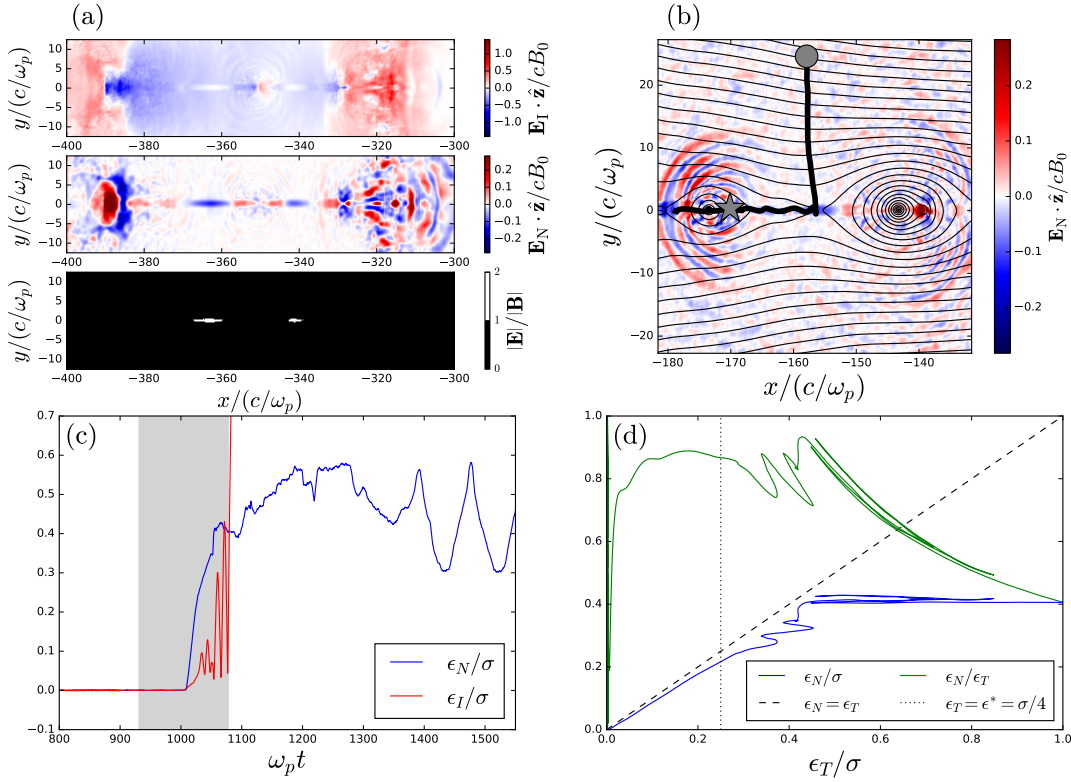


**Figure 1.** (a) Physical quantities from a region of a  $\sigma = 50$  relativistic reconnection simulation: ideal electric field  $\mathbf{E}_I$  (top); nonideal electric field  $\mathbf{E}_N$  (middle); ratio of electric and magnetic field magnitudes with color scaled so that only regions satisfying  $|\mathbf{E}| > |\mathbf{B}|$  are white (bottom). (b) Representative simulation particle trajectory from a  $\sigma = 50$  simulation of relativistic reconnection plotted over the out-of-plane component of the nonideal electric field with overlaid magnetic field lines. The trajectory corresponds to the shaded times in (c), with the circle showing the position at the beginning of this period and the star showing the position at the time when  $\epsilon_T = \sigma/4$ . (c) Evolution of energy gained by the nonideal ( $\epsilon_N$ ) and ideal ( $\epsilon_I$ ) electric fields. (d) Energy gained from the nonideal field ( $\epsilon_N/\sigma$ ) versus total energy ( $\epsilon_T/\sigma$ ) and fractional energy gain from the nonideal electric field,  $\epsilon_N/\epsilon_T$ , vs. total particle energy  $\epsilon_T/\sigma$ .

### 3. RESULTS

We now apply this analysis to a set of 2D simulations with varied magnetization  $\sigma$  and guide field  $B_G$ . All analysis is applied at the end of the simulations at  $\omega_p t \approx 2000$ . The corresponding electron energy spectra are shown in Figure 2 (a), with normalizations shifted for ease of comparison. All spectra show nonthermal components resembling power law distributions  $\sim \epsilon_{\text{final}}^{-\alpha}$  over more than a decade in energy normalized to sigma. The cases with  $B_G = 0$  have power law indices in the range  $\alpha = 2-3$  and maximum particle energies in the range  $\epsilon_{\text{max}}/\sigma \approx 8-20$ . The simulations with finite guide field all have  $\sigma = 50$ , and their power laws become steeper and extend to lower maximum energies as the guide field is increased. The spectrum for the  $\sigma = 200$  is slightly less developed due to the wider current sheet width used which increases the time for reconnection onset. We first focus on the simulation with  $\sigma = 50$  and  $B_G = 0$ . The curves in Figure 2 (b) show the fractional contribution of the nonideal field to the energy gain up to the threshold energy, averaged over all electrons and binned by final particle energy  $\epsilon_{\text{final}}$ :  $(\epsilon_N/\epsilon_T)|_{\epsilon_T=\epsilon^*} = (1/N_p) \sum_{i=1}^{N_p} (\epsilon_{N,i}/\epsilon_{T,i})|_{\epsilon_{T,i}=\epsilon^*}$ . For particles with a given final particle energy  $\epsilon_{\text{final}}$ , the corresponding points on the curves quantify the role of the nonideal field in bringing those particles to the energy  $\epsilon^*$ . Each curve in this panel is obtained from all of the electron data at a single time in the same simulation, but using different values of the threshold energy in the range  $\epsilon^*/\sigma = 1/8 - 2$ . For the smallest threshold energy of  $\epsilon^*/\sigma = 1/8$  (blue curve) the nonideal field begins to dominate for particles with final energies  $\epsilon_{\text{final}} \gtrsim 2\sigma$ , and increases in importance with final particle energy. For the particles

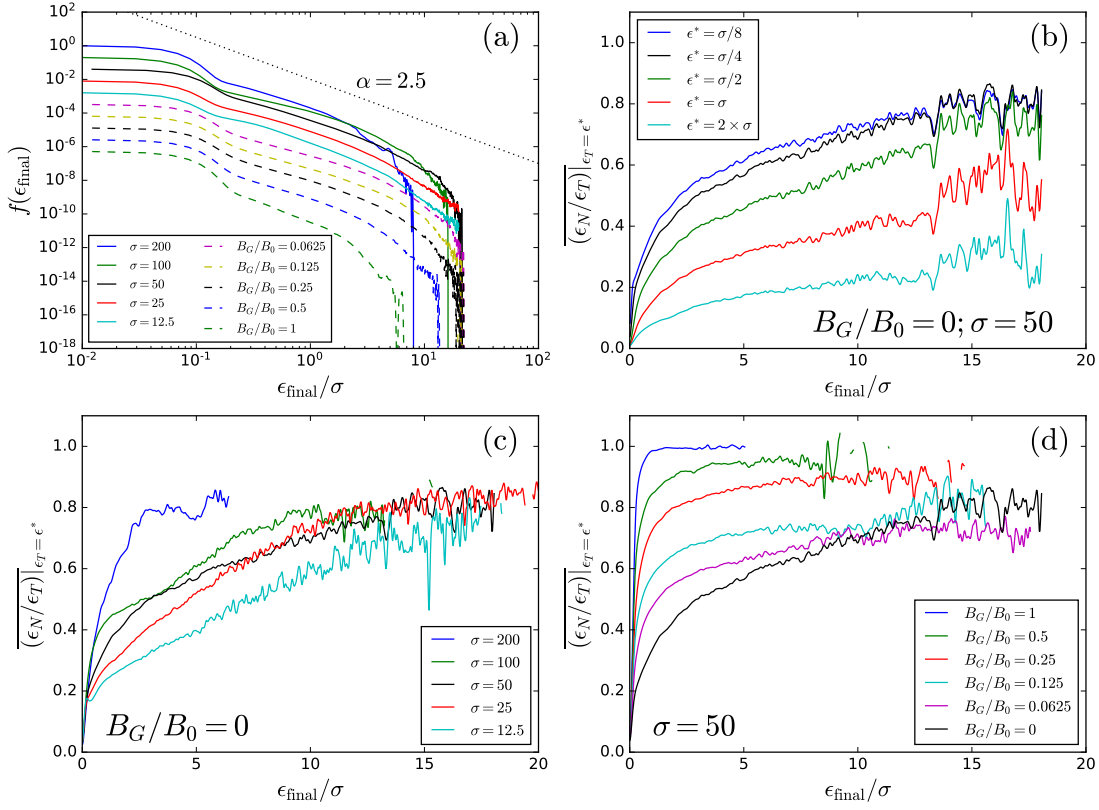


**Figure 2.** (a) Electron energy spectra at the end of the simulation ( $\omega_p t \approx 2000$ ) for various conditions. Solid lines have  $B_G = 0$ , and dashed lines have  $\sigma = 50$  and  $B_G > 0$ . Dotted black line shows a power law spectrum with index  $\alpha = 2.5$  for reference. (b) Average fractional nonideal contribution to energization up to various threshold energies  $\epsilon^*$  for the  $\sigma = 50$ ,  $B_G = 0$  simulation. (c) Average fractional nonideal contribution to energization up to  $\epsilon^* = \sigma/4$  for simulations with varied  $\sigma$  and  $B_G = 0$ . (d) Same as (c), but for  $\sigma = 50$  and varied  $B_G$ . All solid black lines correspond to the 2D simulation with  $\sigma = 50$  and  $B_G = 0$ .

with the highest energy, the nonideal field provided more than 80% of the energy in their initial rise to  $\epsilon_T = \sigma/8$ . As the threshold energy is increased the fraction of energy gained by the nonideal field begins to drop. This indicates the ideal field is primarily responsible for later stages of energization, in accordance with previous expectations. The fraction of energy coming from the nonideal field steeply drops for threshold energies of  $\epsilon^* > \sigma/4$ , which gives evidence of a critical injection energy of  $\epsilon^* \approx \sigma/4$  that allows particles to reach large energies. This trend is confirmed for simulations of  $\sigma = 25$  and  $\sigma = 100$  in addition to the  $\sigma = 50$  case presented in Figure 2 (b). For all of the following analysis, we fix the threshold energy to  $\epsilon^* = \sigma/4$  and refer to energization up to level as injection.

Next we analyze five different simulations with magnetization ranging from  $\sigma = 12.5 - 200$  and zero guide field, with each curve in Figure 2 (c) corresponding to one of these simulations. The nonideal field invariably dominates the injection for the highest energy particles, and shows a trend of increasing importance for higher  $\sigma$ . A similar comparison is shown in Figure 2 (d), now for six simulations with  $\sigma = 50$  and guide field ranging from  $B_G/B_0 = 0 - 1$ . Again, the nonideal field dominates the injection for the highest energy particles in every simulation. For larger guide fields the importance of the nonideal field in injection is seen to sharply increase, with the nonideal field providing nearly 100% of the energy during injection for particles that reach final energies of  $\epsilon_{\text{final}} > \sigma$  for the  $B_G/B_0 = 1$  simulation. The simulations considered thus far have all been 2D, however the current sheet structure and dominant acceleration mechanism are significantly modified in 3D Zhang et al. (2021). The presence of additional kinetic instabilities in 3D which lead to the distortion of flux ropes and turbulence may also be expected to enhance magnetic field diffusion in

the current sheet and thereby strengthen nonideal effects. To understand the influence of 3D effects, we next analyze a 3D simulation with  $\sigma = 50$  and  $B_G = 0$ , shown in Figures 3 (a,b). The 3D simulation has the same size as the 2D simulations in the reconnection plane ( $x - y$ ) that is modeled in 2D, and the resulting electron spectrum shows a similar shape and maximum energy to the analogous 2D case with  $\sigma = 50$  and  $B_G = 0$  at the end of the 3D simulation (Figure 3 (a) inset). In the additional third dimension the size is  $L_z/(c/\omega_p) = 150$ , which is sufficient to capture significant distortion of the flux ropes and disruption of the current sheet, seen in Figure 3 (b). The fraction of injection energy coming from the nonideal field is compared for 2D and 3D in Figure 3 (a), showing how the nonideal field indeed increases in importance in 3D, providing nearly 90% of the injection energy for the highest energy particles and enhanced by 10 – 20% over the 2D case at lower energies.

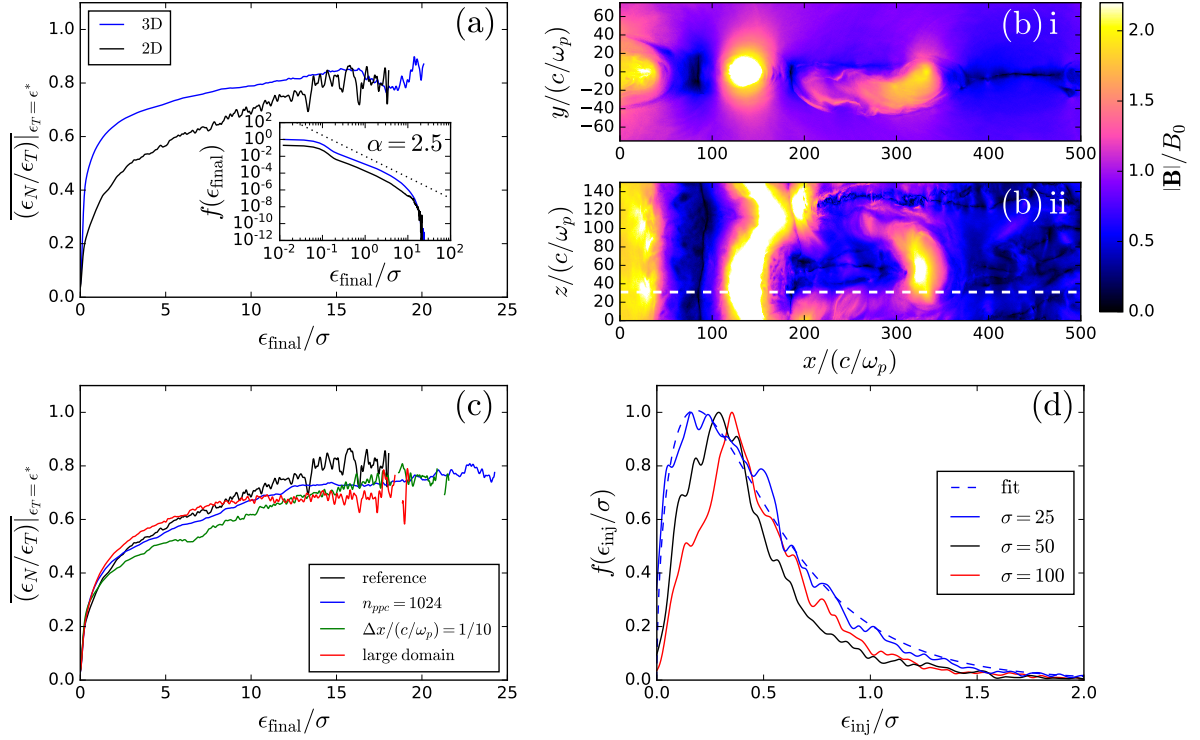


**Figure 3.** (a) Comparison of average fractional contribution of nonideal field to injection for 2D and 3D simulations with  $\sigma = 50$  and  $B_G = 0$ , at time  $\omega_p t \approx 2000$ . Inset shows the corresponding electron energy spectra, with a power law spectrum with index  $\alpha = 2.5$  plotted for reference. (b) Magnetic field magnitude in 2D slices of the 3D simulation at  $\omega_p t \approx 1200$ . (i)  $x - y$  plane at  $z/(c/\omega_p) = 31$ , and (ii)  $x - z$  plane at  $y = 0$  (dashed line shows the location of the  $x - y$  slice). (c) Convergence studies showing the average fractional contribution of the nonideal field to injection for  $\sigma = 50$ ,  $B_G = 0$  simulations with standard parameters (black),  $n_{ppc} = 1024$  (blue),  $\Delta x/(c/\omega_p) = 1/10$  (green), and a domain size of  $L_x/(c/\omega_p) = 2000$  and  $L_y/(c/\omega_p) = 4500$  (red). (d) Distribution of injection energies obtained from simulations with varied sigma. Dashed blue line shows a fit of the  $\sigma = 25$  case to the function  $a\epsilon^b e^{-\epsilon/c}$ . All solid black lines correspond to the 2D simulation with  $\sigma = 50$  and  $B_G = 0$ .

The method of obtaining the nonideal field used in this study relies on calculating fluid quantities by averaging a finite number of simulation particles onto a spatial grid, and thus it is critical to perform convergence studies to ensure the results are not being affected by discrete particle noise or spatial resolution. Figure 3 (c) shows a convergence study of the nonideal injection analysis for 2D simulations with  $\sigma = 50$  and  $B_G = 0$ . When compared to the reference case analyzed previously (black line), the results do not significantly change when increasing the number of particles-per-cell per-species from  $n_{ppc} = 16$  to  $n_{ppc} = 1024$ , or increasing the spatial resolution from  $\Delta x/(c/\omega_p) = 1/4$  to  $\Delta x/(c/\omega_p) = 1/10$ . Finally, it is important to understand if the system size or boundary conditions are influencing the results. To test this we have run a simulation with a domain size of  $L_x/(c/\omega_p) = 2000$  and  $L_y/(c/\omega_p) = 4500$ ,

which is sufficient to ensure light crosses the periodic  $x$  boundaries exactly once over the duration of the simulation and that light traveling from the  $y$  boundaries first reaches the edge of the largest plasmoids only at the end of the simulation. The insensitivity of the results to this change (red curve in Figure 3 (c)) confirms that the boundaries are not influencing the results.

#### 4. DISCUSSION

The analysis presented above definitively demonstrates the critical role of the nonideal electric field in particle injection for relativistic reconnection, providing the dominate source of energy during injection for the wide range of parameters studied. The increase in the importance of the nonideal field with  $B_G$  and in 3D indicates nonideal fields will be responsible for injecting particles in the general physical scenario of arbitrarily aligned magnetic fields in a 3D plasma. Although nonideal fields are by definition beyond those captured in MHD, it may be possible to develop test particle models that approximate the nonideal effects of particle injection and allow the remaining acceleration to come from the ideal fields of MHD. A key component of such a model would be the distribution of injection energies, which can be obtained from the trajectories of PIC simulation particles as the amount of energy gained from the nonideal field at the time when injection ceases and the ideal field takes over as the dominant source of energy. An approximate criteria for determining the end of injection is the time when  $d\epsilon_N/d\epsilon_T = 0$ , which can be calculated for each particle during the simulation to obtain a distribution of injection energies. For the example particle trajectory in Figure 1, the injection energy can be seen to be  $\epsilon_{\text{inj}}/\sigma \approx 0.4$  from panel (d). Figure 3 (d) shows the distribution of injection energies obtained in this way from the electrons for three simulations with varied  $\sigma$ . With increasing  $\sigma$  the peak energy of the distribution shows a modest increase, accompanied by a decrease in the peak width. All peaks are near  $\epsilon_{\text{inj}}/\sigma \approx 1/4$ , consistent with the previous determination from Figure 2 (b) that the critical injection energy is  $\epsilon_{\text{inj}}/\sigma \approx 1/4$ . The distribution can be approximated by a gamma distribution parameterized as  $ae^{b\epsilon}e^{-\epsilon/c}$ , and the dashed line shows the result of a least squares fit to the  $\sigma = 25$  case which yielded  $a = 4.68$ ,  $b = 0.566$ , and  $c = 0.320$ . A full characterization of the distribution of injection energies, its dependence on the plasma conditions, and the incorporation into MHD test particle simulations will be the subject of future work. The present analysis does not distinguish between different sources of nonideal fields, however the same technique could be applied to precisely determine the roles of each term in a generalized Ohm's in different stages of particle acceleration. This would be particularly valuable for connecting to high-moment fluid models Hakim (2008); Dong et al. (2019); Ng et al. (2020); Wang et al. (2018). Finally, we note that the convergence studies demonstrate the soundness and computational feasibility of this novel analysis method, which can now be applied more broadly to other particle acceleration scenarios such as collisionless shock waves, turbulence, and relativistic jets.

#### 5. CONCLUSIONS

In conclusion, we have performed the first self-consistent analysis of the energization from ideal and nonideal electric fields from relativistic reconnection within fully kinetic PIC simulations. We have done so by rigorously separating nonideal and ideal electric fields from first principles without adopting ad hoc definitions of the nonideal field. We find the nonideal field is the dominate source of energy for particles during the injection process, with later energization coming from the ideal field. The importance of the nonideal field for injection increases with  $\sigma$ ,  $B_G$ , and in 3D, indicating the general relevance of these results for relativistic reconnection in nature. We obtain the statistical distribution of injection energies from the simulation particles, which may be incorporated into extended test particle MHD models that allow accurate simulation of particle acceleration in large-scale astrophysical systems. Convergence studies demonstrate the validity of this novel analysis method, which may now be applied to yield new insight into a wide variety of plasma processes.

#### 6. ACKNOWLEDGMENTS

This project was supported by the International Research Collaboration Center, Astro-fusion Plasma Physics (IRCC-AFP) program of the National Institutes of Natural Sciences (NINS), Japan. S.T. and A.B. acknowledge gratefully the support of NSF Awards 2206756 and 2209471. A part of this research was supported by JSPS KAKENHI (S.Z.: 21K03627; S.M.: 22H01287; M.M.: 19K03916, 20H01941, 22H01272). Simulations were performed on Perlmutter (NERSC). The authors acknowledge the OSIRIS Consortium, consisting of UCLA and IST (Portugal) for the use of the OSIRIS 4.0 framework. We thank R. Matsumoto, K. Tomida, and M. Hoshino for valuable discussions.

## REFERENCES

- Birdsall, C., & Langdon, A. 1985, *Plasma Physics via Computer Simulation* (McGraw-Hill)
- Dong, C., Wang, L., Hakim, A., et al. 2019, *Geophysical Research Letters*, 46, 11584
- Drake, J. F., Swisdak, M., Che, H., & Shay, M. A. 2006, *Nature*, 443, 553.  
<http://www.ncbi.nlm.nih.gov/pubmed/17024088>
- Fonseca, R. A., Martins, S. F., Silva, L. O., et al. 2008, *Plasma Physics and Controlled Fusion*, 50, 124034.  
<http://arxiv.org/abs/0810.2460>
- Fonseca, R. A., Vieira, J., Fiuza, F., et al. 2013, *Plasma Physics and Controlled Fusion*, 55, 124011.  
<http://stacks.iop.org/0741-3335/55/i=12/a=124011?key=crossref.96a8cddb9b5024abacb36e3d8610727>
- Fonseca, R. A., Silva, L. O., Tsung, F. S., et al. 2002, *Lect. Notes Comput. Sci.*, 2331, 342. [http://link.springer.com/chapter/10.1007/3-540-47789-6\\_36](http://link.springer.com/chapter/10.1007/3-540-47789-6_36)
- Guo, F., Li, H., Daughton, W., & Liu, Y. H. 2014, *Physical Review Letters*, 113, 1. <http://arxiv.org/abs/1405.4040>
- Guo, F., Li, X., Daughton, W., et al. 2019, *The Astrophysical Journal*, 879, L23
- Guo, F., Li, X., French, O., et al. 2022, arXiv
- Hakim, A. H. 2008, *Journal of Fusion Energy*, 27, doi:10.1007/s10894-007-9116-z
- Hesse, M., Neukirch, T., Schindler, K., Kuznetsova, M., & Zenitani, S. 2011, *Space Science Reviews*, 160, doi:10.1007/s11214-010-9740-1
- Ji, H., & Daughton, W. 2011, *Physics of Plasmas*, 18, 111207
- Kilian, P., Li, X., Guo, F., & Li, H. 2020, *The Astrophysical Journal*, 899, 151
- Ng, J., Hakim, A., Wang, L., & Bhattacharjee, A. 2020, *Physics of Plasmas*, 27, doi:10.1063/5.0012067
- Oka, M., Phan, T.-D., Krucker, S., Fujimoto, M., & Shinohara, I. 2010, *The Astrophysical Journal*, 714, 915.  
<http://arxiv.org/abs/1004.1154>
- Sironi, L. 2022, *Physical Review Letters*, 128, 145102
- Sironi, L., & Spitkovsky, A. 2014, *The Astrophysical Journal*, 783, L21.  
<http://iopscience.iop.org/2041-8205/783/1/L21>
- Wang, L., Germaschewski, K., Hakim, A., et al. 2018, *Journal of Geophysical Research: Space Physics*, 123, doi:10.1002/2017JA024761
- Yamada, M., Kulsrud, R., & Ji, H. 2010, *Reviews of Modern Physics*, 82, 603.  
<http://link.aps.org/doi/10.1103/RevModPhys.82.603>
- Zenitani, S. 2018, *Plasma Physics and Controlled Fusion*, 60, 014028
- Zenitani, S., & Hoshino, M. 2001, *The Astrophysical Journal*, 562, L63
- Zhang, H., Sironi, L., & Giannios, D. 2021, *The Astrophysical Journal*, 922, 261
- Zweibel, E. G., & Yamada, M. 2009, *Annual Review of Astronomy and Astrophysics*, 47, 291.  
<http://www.annualreviews.org/doi/abs/10.1146/annurev-astro-082708-101726>